Exploration of the bond angle and charge carrier density by rare-earth doping in Sr_2IrO_4

Hui Huang [1,2] Ping Ji,[2] Yu Xie,[2] Hui Han,[1] and Binghui Ge [1,3,*]

[1]*Key Laboratory of Structure and Functional Regulation of Hybrid Materials of Ministry of Education, Institutes of Physical Science and Information Technology, Anhui University, Hefei 230601, China*

[2]*School of Advanced Manufacture and Engineering, Hefei University, Hefei 230601, China*

[3]*Beijing National Laboratory for Condensed Matter Physics, Institute of Physics, Chinese Academy of Sciences, Beijing, 100190, China*

(Received 16 June 2020; revised 25 August 2020; accepted 29 October 2020; published 16 November 2020)

Doping at the Sr site in Sr_2IrO_4 is predicted to be a possible route to high-temperature superconductivity, which has not yet been experimentally achieved. We have made a comprehensive investigation on the interplay among the Ir-O-Ir bond angle, carrier density, and magnetic and transport properties of rare-earth-doped Sr_2IrO_4 by choosing Pr and Ce as the dopants. We find that compared with Pr doping, Ce doping introduces more effective charge carriers into the Sr_2IrO_4 matrix, leading to a more rapid suppression of its magnetic ordering. A metallic-like behavior has been observed in heavily Ce-doped samples. The evolutions of magnetic and transport behaviors are found to be less relevant to the distorted Ir-O-Ir bond angle. The present results suggest that the charge carrier density could be a crucial factor in determining the physical properties of rare-earth-doped Sr_2IrO_4 compounds.

DOI: 10.1103/PhysRevMaterials.4.115001

I. INTRODUCTION

Superconductivity is a fascinating phenomenon, where two charge carriers near the Fermi energy can be combined into so-called Cooper pairs. The glue of Cooper pairs in conventional superconductors is the phonon-mediated attractive interaction between carriers. However, in high-temperature superconductors such as cuprate oxide and iron-based superconductors [1–3], it seems that the phonon-mediated interaction cannot account for such high transition temperatures in these materials. Nowadays, the understanding of the underlying mechanisms that govern the phase transition from the long-range ordered antiferromagnetic insulating state into the superconducting state upon charge carrier doping in these 3*d* transition metal oxides remains a big challenge. For both cuprate oxide and iron-based superconductors, various experimental techniques have been utilized in order to reveal their physical properties from structural, transport, and magnetic as well as other aspects [4–8]. However, it seems that no consensus can be reached regarding the underlying superconducting mechanisms in high-temperature superconductors at present. Thus it is widely expected to find a new class of high-temperature superconducting materials, which is believed to be helpful in the final establishment of high-temperature superconducting mechanisms.

In recent years, 5*d* transition metal oxide Sr_2IrO_4 has attracted considerable attention due to its unusual $J_{\text{eff}}=\frac{1}{2}$ state leaded Mott-like insulating ground state [9–13]. This ground state, together with the similarities in the crystal structures and magnetic states of Sr_2IrO_4 with the parent compound of cuprate superconductor La_2CuO_4, make Sr_2IrO_4 a promising material platform for exploring possible high-temperature superconductivity. As expected, theoretical calculations of the band structures and the ground-state phase diagram suggest possible unconventional high-temperature superconductivity upon carrier doping in this material [14–18]. Guided by the theoretical predications, the experimental exploration of superconductivity in doped Sr_2IrO_4 looks like a very easy task. However, despite extensive investigations with doped Sr_2IrO_4 [18–25], the observation of bulk superconductivity remains unsuccessful. In addition, a recent investigation on Sr_2IrO_4 reveals a persistent insulating state at megabar pressures [26]. These results are in sharp contrast with the situations in doped La_2CuO_4, where only small amount of Ba or Sr doping could lead to the depression of magnetic ordering and the transition from an insulating state into superconducting state.

In order to effectively explore possible high-temperature superconductivity in doped Sr_2IrO_4, one needs to know why the insulating state is so robust in this compound. Previous investigations of doped Sr_2IrO_4 have revealed three main features which are different from the cases in doped La_2CuO_4 [18–25]: The first one is that the effective charge carrier concentration in doped Sr_2IrO_4 is very low. The second is that a large rotation of IrO_6 octahedra persists, leading to a significantly distorted in-plane Ir-O-Ir bond angle. The last is that a short-range antiferromagnetic-ordered state survives even at a very high doping level. How to overcome these problems, and what is the most important factor which renders the occurrence of superconductivity, are awaiting comprehensive investigation. In this work, we perform a systematic investigation of detailed lattice parameters, the doping introduced charge carrier concentration and magnetic and transport properties of two series of Pr- and Ce-doped Sr_2IrO_4 samples. From detailed analysis of crystal structure and electronic and magnetic properties we suggest that the distorted Ir-O-Ir bond

*bhge@iphy.ac.cn

angle may not be an insurmountable barrier in controlling the physical properties of Sr_2IrO_4 compounds. If one can introduce sufficient charge carriers into the Sr_2IrO_4 matrix, the magnetic and transport behaviors could be substantially changed, despite the existence of largely distorted Ir-O-Ir bond angle. The present results could be informative for future exploration of possible high-temperature superconductivity in Sr_2IrO_4 compounds.

II. EXPERIMENT

Polycrystalline samples of $Sr_{2-x}Pr_xIrO_4$ and $Sr_{2-x}Ce_xIrO_4$ were prepared using a conventional solid-state reaction technique. Previous studies on rare-earth doping in Sr_2IrO_4 revealed a small amount of impurity phases when the doping level is higher than $x = 0.15$, indicating that the rare-earth atoms are not easy to be incorporated into the Sr_2IrO_4 lattice [21,22]. In this work, we attempted to improve the reaction by slightly increase the calcining temperature of the doped samples. In detail, stoichiometric powders of $SrCO_3$ (99.9%), IrO_2 (99.9%), Pr_6O_{11} (99.99%), and CeO_2 (99.99%) were mixed and thoroughly ground as the starting materials. Before the weighing of Pr_6O_{11} and CeO_2, these starting materials were dried at 800 °C for 12 h in order to dehydrate the absorbing water. Then the mixed powders were directly heated to 1250 °C and maintained at that temperature for one day. After an intermediate grinding, the powders were preheated at 1250 °C for another day. Then the materials were pressed into pellets for the final calcining. The final calcining temperature was increased from 1250 °C for the $x \leqslant 0.05$ samples to 1270 °C for the $0.1 \leqslant x \leqslant 0.15$ samples and finally to 1290 °C for the $x \geqslant 0.2$ samples. The final calcining was performed for two days. The phase purity of the samples was checked by powder x-ray diffraction (XRD) on a Rigaku-TTR3 x-ray diffractometer using Cu Kα radiation. Rietveld refinement was performed on the collected XRD data using the GSAS software package [27]. The actual compositions of the samples were determined using energy dispersive x-ray spectrometry (EDX) performed on an Oxford Swift 3000 spectrometer equipped with a Hitachi TM3000 scanning electron microscope. The applied accelerating voltage to the electron beam was 5 keV during the EDX measurements, and the surfaces of the samples were carefully polished in order to avoid self-absorption effects. The longitudinal and transverse resistivity was measured using a standard four-probe method taken on a Quantum Design Physical Property Measurement System. Magnetic properties were investigated using a superconducting quantum interference device magnetometer.

III. RESULTS AND DISCUSSION

First we need to know to what extent the chosen elements Pr and Ce are incorporated into Sr_2IrO_4 compounds. We perform an energy-dispersive x-ray spectrometry (EDX) analysis on the $Sr_{2-x}Pr_xIrO_4$ and $Sr_{2-x}Ce_xIrO_4$ samples. For each sample, we randomly select 20 points to perform the EDX measurement, and the average has been adopted as the real composition of the sample. Table I gives the comparison of the nominal compositions and the actual compositions of the two series of doped Sr_2IrO_4 samples. It is found that at low doping content ($x \leqslant 0.1$), the actual compositions and the nominal compositions are comparable. However, at high doping content, the actual doping contents are apparently less than the nominal doping contents in both Pr- and Ce-doped samples. It can be concluded that the solid solubility of Pr and Ce in the $Sr_{2-x}A_xIrO_4$ (A = Pr, Ce) compound is about $x = 0.22$ and 0.21, respectively.

TABLE I. The comparison between nominal and real compositions of the $Sr_{2-x}A_xIrO_4$ (A = Pr, Ce) compounds, determined by EDX measurement. Here the oxygen content is not included in the EDX analysis.

Nominal composition	Real composition
Sr_2IrO_4	$Sr_{2.004\pm0.007}IrO_4$
$Sr_{1.98}Pr_{0.02}IrO_4$	$Sr_{1.982\pm0.007}Pr_{0.021\pm0.002}IrO_4$
$Sr_{1.95}Pr_{0.05}IrO_4$	$Sr_{1.949\pm0.005}Pr_{0.052\pm0.003}IrO_4$
$Sr_{1.9}Pr_{0.1}IrO_4$	$Sr_{1.902\pm0.006}Pr_{0.096\pm0.003}IrO_4$
$Sr_{1.85}Pr_{0.15}IrO_4$	$Sr_{1.858\pm0.004}Pr_{0.145\pm0.005}IrO_4$
$Sr_{1.8}Pr_{0.2}IrO_4$	$Sr_{1.808\pm0.004}Pr_{0.189\pm0.006}IrO_4$
$Sr_{1.7}Pr_{0.3}IrO_4$	$Sr_{1.753\pm0.007}Pr_{0.212\pm0.009}IrO_4$
$Sr_{1.98}Ce_{0.02}IrO_4$	$Sr_{1.983\pm0.005}Ce_{0.020\pm0.002}IrO_4$
$Sr_{1.95}Ce_{0.05}IrO_4$	$Sr_{1.955\pm0.005}Ce_{0.049\pm0.003}IrO_4$
$Sr_{1.9}Ce_{0.1}IrO_4$	$Sr_{1.907\pm0.006}Ce_{0.094\pm0.003}IrO_4$
$Sr_{1.85}Ce_{0.15}IrO_4$	$Sr_{1.854\pm0.006}Ce_{0.142\pm0.004}IrO_4$
$Sr_{1.8}Ce_{0.2}IrO_4$	$Sr_{1.822\pm0.006}Ce_{0.183\pm0.007}IrO_4$
$Sr_{1.7}Ce_{0.3}IrO_4$	$Sr_{1.768\pm0.008}Ce_{0.207\pm0.009}IrO_4$

Figures 1(a) and 1(b) show the powder XRD patterns of the $Sr_{2-x}Pr_xIrO_4$ and $Sr_{2-x}Ce_xIrO_4$ samples, respectively. Overall, the main peaks exhibited in Fig. 1 can be well indexed based on a tetragonal cell structure with the $I4_1/acd$ space

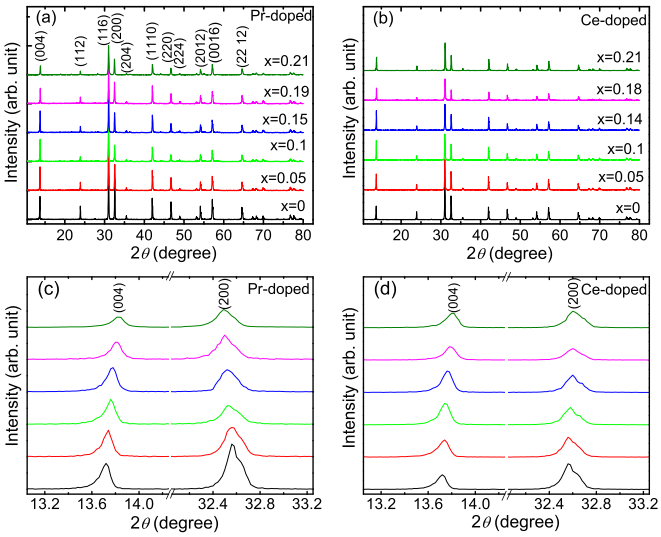

FIG. 1. (a) X-ray diffraction patterns of the $Sr_{2-x}Pr_xIrO_4$ samples. The Miller indices corresponding to the diffraction peaks are marked according to an $I4_1/acd$ space group. (b) X-ray diffraction patterns of the $Sr_{2-x}Ce_xIrO_4$ samples. (c) and (d) An enlarged view of the (004) and (200) peaks for the (c) $Sr_{2-x}Pr_xIrO_4$ and (d) $Sr_{2-x}Ce_xIrO_4$ samples.

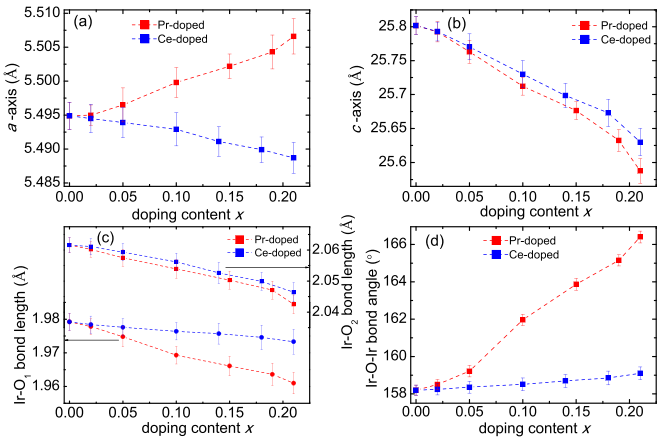

FIG. 2. (a) The doping dependence of the a-axis lattice parameter for the $Sr_{2-x}A_xIrO_4$ (A = Pr, Ce) samples. (b) The doping dependence of the c-axis lattice parameter. (c) The variation of in-plane Ir-O_1 bond distance and out-of-plane Ir-O_2 bond distance for the $Sr_{2-x}A_xIrO_4$ (A = Pr, Ce) samples. (c) The variation of in-plane Ir-O_1-Ir bond angle with Pr and Ce doping.

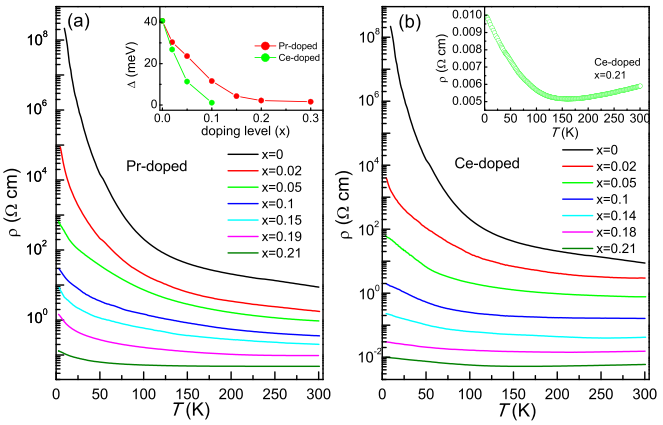

FIG. 3. Temperature dependence of resistivity of $Sr_{2-x}Pr_xIrO_4$ (a) and $Sr_{2-x}Ce_xIrO_4$ (b) samples. The insets show the variation of the energy gap with increasing rare-earth element doping.

group. No impurity peaks can be found in both series of XRD patterns when the Pr and Ce doping content is less than $x = 0.18$. For the $x = 0.21$ samples, some weak impurity peaks could be observed, probably meaning that small amount of Pr_6O_{11} and CeO_2 is not reacted in these samples. It is found that the phase purity can be substantially improved by slightly increasing the calcining temperature. In order to learn in detail the shift of the diffraction peaks with rare-earth doping, we give an enlarged view of the (004) and (200) peaks for the $Sr_{2-x}Pr_xIrO_4$ [Fig. 1(c)] and $Sr_{2-x}Ce_xIrO_4$ [Fig. 1(d)] samples. For $Sr_{2-x}Pr_xIrO_4$, it is found that the position of the (004) peak gradually shifts to a higher angle with increasing Pr doping. For the (200) peak, the position shifts to a lower angle. These results indicate an increase of the a-axis lattice parameter and a decrease of the c-axis lattice parameter in the Pr-doped samples. For the $Sr_{2-x}Ce_xIrO_4$, we find that both (004) and (200) peaks monotonously shift to a higher angle, suggesting the decrease of both a and c lattice constants in Ce-doped samples.

From the XRD patterns it is found that the doping of Pr and Ce results in a different response of the a-axis lattice parameter. Ir order to reveal the variations of lattice parameters with rare-earth doping, we perform a detailed Rietveld refinement on the XRD data of the $Sr_{2-x}A_xIrO_4$ (A = Pr, Ce) samples. Figure 2(a) depicts the variations of a-axis lattice parameters with Pr and Ce doping. It is clear that the a-axis lattice constant monotonously increases with increasing Pr doping content, while it decreases with increasing Ce doping content. The different response of a-axis lattice constant on Pr and Ce doping is unexpected, as both the Pr (1.65 Å) and Ce (1.65 Å) atoms have smaller covalent radii than that of Sr (1.91 Å). In fact, previous investigations on the La, Ga, and Sm doping in Sr_2IrO_4 all reveal an increase of the a-axis lattice constant [19–21]. From Fig. 2(b) it is found that the c-axis lattice constant decreases monotonously with increasing doping content in both Pr-doping and Ce-doping samples. The variations of the a- and c-axis lattice parameters would be closely related to the changes in the Ir-O and Sr(Pr,Ce)-O bond distances and bond angles. In Sr_2IrO_4, the distorted IrO_6 octahedra in the center part of the crystal lattice are the crucial lattice factor which determine the physical behaviors of the materials. Figure 2(c) shows the doping dependence of the in-plane Ir-O_1 bond distance and the out-of-plane Ir-O_2 bond distance of the Pr- and Ce-doped samples. It is found that both the Ir-O_1 bond distance and the Ir-O_2 bond distance decrease monotonously with increasing doping content in the two series of samples, indicating a shrinkage of the IrO_6 octahedra. A noticeable feature is that the Ir-O_1 bond distance decreases more rapidly in the Pr-doped samples than that in Ce-doped samples. This fact seems to be inconsistent with the fact that the Pr doping leads to an increase in the in-plane a-axis lattice constant. The only possible reason is that there is a substantial straightening of the in-plane Ir-O_1-Ir bond angle in Pr-doped samples. Thus in Fig. 2(d) we plot the variation of the Ir-O_1-Ir bond angle with doping. It is clear that the Pr doping results in a significant increase of the in-plane Ir-O_1-Ir bond angle. This increased Ir-O_1-Ir bond angle can account for the increased a-axis lattice constant and the decreased Ir-O_1 bond distance. For the Ce-doped samples, the doping also leads to a slight increase in the in-plane Ir-O_1-Ir bond angle, but it is much less than that in Pr-doped ones.

Figure 3 shows the temperature dependence of resistivity of the $Sr_{2-x}Pr_xIrO_4$ [Fig. 3(a)] and $Sr_{2-x}Ce_xIrO_4$ [Fig. 3(b)] samples. The parent compound Sr_2IrO_4 exhibits a typical insulating behavior in the whole temperature range, which is consistent with previous reports [9]. With the corporation of Pr and Ce, a systematic decrease of resistivity has been found in both the $Sr_{2-x}Pr_xIrO_4$ and $Sr_{2-x}Ce_xIrO_4$ samples. It is worthwhile to notice that the decrease of resistivity is much faster in the Ce-doped samples than in Pr-doped sample. For example, the room temperature resistivity decreases by more than three orders of magnitude in the $Sr_{1.77}Ce_{0.21}IrO_4$ sample, while it decreases by only two orders of magnitude in the $Sr_{1.76}Pr_{0.21}IrO_4$ sample, compared to that of undoped Sr_2IrO_4. In Pr-doped cases, though the resistivity decreases with increasing doping content, all the samples still display an insulating (or semiconducting) behavior. We find that the $\rho \sim T$ curves can be well fitted according to the

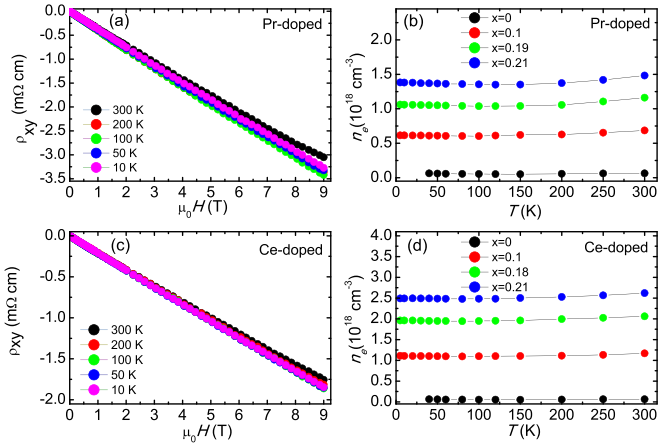

FIG. 4. (a) Transverse resistivity ρ_{xy} versus magnetic field $\mu_0 H$ at different temperatures of the $Sr_{1.76}Pr_{0.21}IrO_4$ sample. The magnetic field is applied perpendicular to the surface of the bulk sample. (b) Estimated temperature dependence of charge carrier concentration for the $Sr_{2-x}Pr_xIrO_4$ samples. (c) The $\rho_{xy} \sim H$ curves of the $Sr_{1.77}Ce_{0.21}IrO_4$ sample. (d) The charge carrier concentration for the $Sr_{2-x}Ce_xIrO_4$ samples.

$\rho(T) = \rho_0 \exp(\Delta/k_B T)$ formula from the 300 K to 80 K region, where Δ and k_B are the energy gap and Boltzmann constant, respectively. Therefore, the energy gap can be obtained from the slope of the straight line, which is fitted to $\ln(\rho) \sim 1/T$ curves. The resultant energy gaps for the Pr-doped samples are plotted in the inset of Fig. 3(a). For the undoped Sr_2IrO_4, the energy gap is about 40.6 meV. It is found that the energy gap systematically decreases with increasing Pr doping. The energy gap reaches about 1.6 meV in $Sr_{1.76}Pr_{0.21}IrO_4$ sample. The energy gap decreases more rapidly in Ce-doped samples than that in Pr-doped samples [the inset of Fig. 3(a)]. In $Sr_{1.9}Ce_{0.1}IrO_4$ sample, the energy gap is about 1.1 meV. When the Ce-doping content is larger than $x = 0.1$, the energy gap disappears and a metallic-like behavior emerges at high temperature. The inset of Fig. 3(b) displays the temperature dependence of resistivity of the $Sr_{1.77}Ce_{0.21}IrO_4$ sample, which shows that the sample exhibits metallic-like conductivity in the 160 K∼300 K region and semiconducting-like conductivity below 160 K.

In both cuprate and iron-based high temperatures, the parent materials exhibit insulating behaviors. With the elemental substitution at the charge reservoir layers, effective charge carriers are introduced into the conductive layers and the insulating-metal transition occurs, eventually leading to the occurrence of a superconducting transition. In Sr_2IrO_4, Pr and Ce are chosen to be incorporated into the $(Sr,Pr,Ce)_2O_2$ charge reservoir layers. It is informative to know how many charge carriers are introduced into the $Sr_{2-x}A_xIrO_4$ (A = Pr, Ce) lattice. We perform an investigation of the Hall coefficients of the $Sr_{2-x}A_xIrO_4$ (A = Pr, Ce) samples from 300 K to 4 K. Figure 4(a) shows the magnetic field dependence of transverse resistivity ρ_{xy} ($\rho_{xy} \sim H$) of the $Sr_{1.76}Pr_{0.21}IrO_4$ sample at different temperatures, with the magnetic field perpendicular to the surface of the sample. The transverse resistivity yields a negative value at all temperatures, suggesting that the transport behaviors are predominantly contributed by electron-type charge carriers. A quasilinear behavior of $\rho_{xy} \sim H$ curves has been observed, probably meaning that the $Sr_{2-x}Pr_xIrO_4$ samples can be described by a single-band-like Fermi surface. The charge carrier density of the $Sr_{2-x}Pr_xIrO_4$ samples is determined using $n = H/\rho_{xy}e$. The resultant variations of carrier density with temperature and doping in $Sr_{2-x}Pr_xIrO_4$ samples are plotted in Fig. 4(b). The carrier density of the undoped Sr_2IrO_4 is about 6×10^{16} cm^{-3}, which is consistent with its insulating behavior. With the incorporation of Pr, the carrier density is significantly increased. For example, the carrier density at room temperature is about 7×10^{17} cm^{-3} for the $Sr_{1.9}Pr_{0.1}IrO_4$ sample, which is one order of magnitude larger than that of the undoped sample. At room temperature, the carrier density eventually reaches to 1.5×10^{18} cm^{-3} in the $Sr_{1.76}Pr_{0.21}IrO_4$ sample. With decreasing temperature, the carrier density first decreases slightly and then exhibits a small increase below 120 K. The $\rho_{xy} \sim H$ curves of the $Sr_{1.77}Ce_{0.21}IrO_4$ sample shown in Fig. 4(c) display similar features as those of $Sr_{1.76}Pr_{0.21}IrO_4$. However, from Fig. 4(d) it can be seen that the carrier density is much larger in $Sr_{2-x}Ce_xIrO_4$ samples than that in $Sr_{2-x}Pr_xIrO_4$ samples. For example, the room temperature charge carrier concentration of the $Sr_{1.9}Ce_{0.1}IrO_4$ sample is 1.16×10^{17} cm^{-3}, which is nearly two times that in $Sr_{1.9}Pr_{0.1}IrO_4$ sample. The room temperature carrier density is 2.62×10^{18} cm^{-3} in the $Sr_{1.77}Ce_{0.21}IrO_4$ sample. These facts suggest that the doping of Ce can introduce more charge carriers than the doping of Pr at the same doping level. If we compare the carrier density of the Pr- and Ce-doped Sr_2IrO_4 with that of $La_{2-x}Sr_xCuO_4$, we find that the carrier density in doped Sr_2IrO_4 is much lower than that of $La_{2-x}Sr_xCuO_4$. For example, the hole-type carrier concentration in $La_{1.85}Sr_{0.15}CuO_4$ is about 6.0×10^{21} cm^{-3}, which is at least three orders of magnitude larger than the carrier density in both the Pr- and Ce-doped Sr_2IrO_4. Thus it is concluded that the efficiency of doping is quite low in Sr_2IrO_4 compounds. This low efficiency of doping can well explain the robustness of the insulating state in this material.

Figures 5(a) and 5(b) show the temperature dependence of magnetic susceptibilities of the $Sr_{2-x}Pr_xIrO_4$ samples [Fig. 5(a)] and $Sr_{2-x}Ce_xIrO_4$ samples [Fig. 5(b)] measured under the zero-field-cooling (ZFC) process and field-cooling (FC) process. For the undoped Sr_2IrO_4, it undergoes a ferromagnetic (FM)-like transition below $T_c = 240$ K, below which the magnetic state has been determined to be canted antiferromagnetism [9]. A significant difference between the ZFC magnetic susceptibility and FC curve has been observed below T_c, indicating a net ferromagnetic moment in the ordered magnetic state. With the corporation of Pr and Ce, the transition temperature is decreased and the magnetic susceptibility is suppressed, suggesting that the magnetic order has been suppressed by the rare-earth doping. In the Pr-doped samples, a weak FM transition can be found below ∼25 K even in the $x = 0.21$ sample, indicating that the magnetic order exists in all Pr-doped samples. In the Ce-doped samples, no apparent FM transition has been found in the $x = 0.21$ sample, probably suggesting that the static magnetic order is completely suppressed. These facts suggest that the Ce doping leads to a more rapid suppression of the magnetic order comparing to Pr doping.

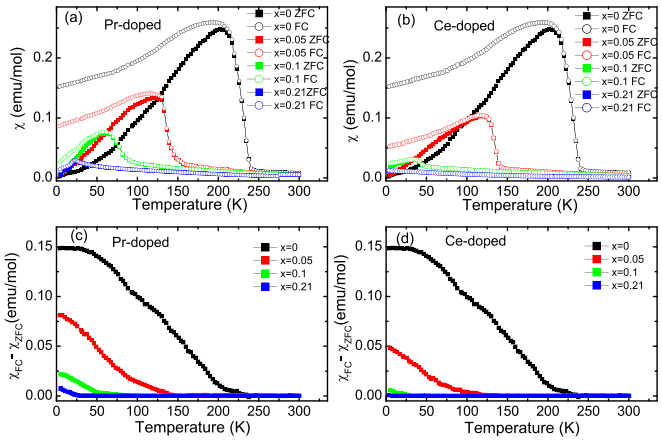

FIG. 5. (a) Temperature dependence of magnetic susceptibilities of the $Sr_{2-x}Pr_xIrO_4$ samples measured under the zero-field-cooling (ZFC) process and field-cooling (FC) process. The applied magnetic field is 1 kOe. (b) The magnetic susceptibilities of the $Sr_{2-x}Ce_xIrO_4$ samples. (c) and (d) The substraction of FC and ZFC data for the $Sr_{2-x}Pr_xIrO_4$ samples (c) and $Sr_{2-x}Ce_xIrO_4$ samples (d).

In order to characterize the evolution of magnetic order, the irreversibility of the magnetic susceptibility data has been obtained by subtracting the ZFC susceptibility from the FC data. The resultant irreversibility curves of the $Sr_{2-x}Pr_xIrO_4$ samples and $Sr_{2-x}Ce_xIrO_4$ samples are shown in Figs. 5(c) and 5(d), respectively. Two features are found. One is that the onset of the irreversibility shifts to low temperatures with the increasing of rare-earth doping. The other is that the magnitude of the irreversibility data rapidly decreases with increasing doping.

Based on the temperature dependence of magnetic susceptibility and resistivity data, we plot in Fig. 6 the phase diagrams of the $Sr_{2-x}Pr_xIrO_4$ samples and $Sr_{2-x}Ce_xIrO_4$ samples. From Fig. 6(a) it can be seen that the corporation of Pr results in a substantial depression of the ordered magnetic state. The transition from high-temperature paramagnetism to canted antiferromagnetic state has been driven to a low temperature with increasing Pr doping. The static magnetic order persists in all samples. The Pr-doped samples all exhibit

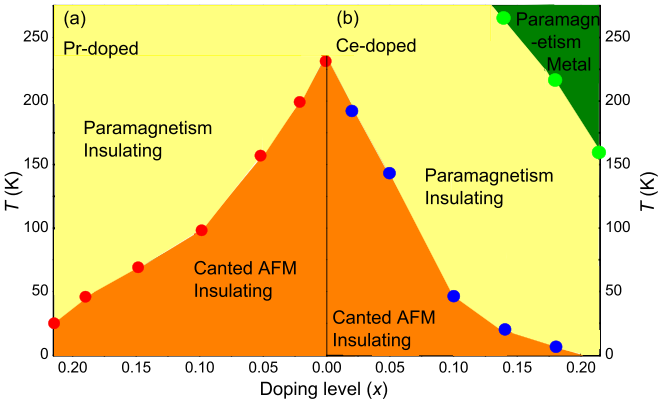

FIG. 6. The phase diagrams of the $Sr_{2-x}Pr_xIrO_4$ samples (a) and $Sr_{2-x}Ce_xIrO_4$ samples (b), showing the evolutions of magnetic order and the conduction behaviors of Sr_2IrO_4 with doping.

insulating (or semiconducting)-like behavior in the whole temperature regions. For the Ce-doped cases, the evolutions of magnetic and conduction behaviors are different from those in Pr-doped ones. For examples, the static magnetic order has been completely depressed in Ce-doped samples when the doping level is high than $x = 0.18$, and a metallic-like behavior has been observed in $x \geqslant 0.14$ samples.

Guided by the theoretical predictions that electron doping in Sr_2IrO_4 could be a possible route to high-temperature superconductivity, Sr_2IrO_4 compounds have been extensively investigated in recent years. The puzzling issue is that the insulating state in Sr_2IrO_4 is very robust, which is in contrast with that in La_2CuO_4 where the application of pressure or chemical doping could easily lead to insulating-to-metal transition. The distorted IrO_6 octahedra and the rotation of bond angles are thought to be especially important for determining the magnetic ground state in Sr_2IrO_4 due to large spin-orbit coupling combined with extended orbitals [28]. However, whether or not the distorted Ir-O-Ir bonds are the key factors in determining the transport behaviors in doped Sr_2IrO_4 is still unclear. In fact, in the prototype high-temperature superconductor $La_{2-x}Sr_xCuO_4$, the in-plane Cu-O-Cu bond is slightly deviated from a straight line in the undoped La_2CuO_4. With Sr or Ba doping, the Cu-O-Cu bond angle increases, and an insulating-to-metal transition occurs. In the Sr_2IrO_4, the distortion on the in-plane Ir-O-Ir bond is significantly larger than that of the Cu-O-Cu bond in La_2CuO_4. Thus it is natural to guess that the severely distorted Ir-O-Ir bond prevents the expected onset of metallization [26]. In the present work, we find that the distorted Ir-O-Ir may not be so important in determining the transport behavior of doped Sr_2IrO_4. Such an argument is based on the fact that a metallic-like behavior is found in Ce-doped samples where the Ir-O-Ir bond angle is severely distorted, while a robust insulating-like conductivity behavior has been observed in Pr-doped samples where the distortion of Ir-O-Ir bond is significantly released. If sufficient charge carriers are introduced, the static magnetic ordering can be suppressed, leading to a metallic-like conductive behavior. A noticeable fact is that the charge carrier concentration is at the 10^{18} cm^{-3} level in $Sr_{2-x}A_xIrO_4$ (A = Pr, Ce) compounds, which is three orders of magnitude less than that in $La_{2-x}Sr_xCuO_4$ superconductor. In the future, how to introduce more charge carriers into the Sr_2IrO_4 matrix is the most important problem in exploring possible high-temperature superconductivity in this compound.

IV. CONCLUSION

In summary, we report a systematic comparison of the lattice structure and the magnetic and transport behaviors between Pr- and Ce-doped Sr_2IrO_4 samples. The Ir-O-Ir bond angle is substantially straightened in Pr-doped samples, while it is less changed in Ce-doped ones. Interestingly, we notice that the static magnetic ordering is more rapidly suppressed in Ce-doped samples than that in Pr-doped ones, and a metallic-like conductivity is observed in Ce-doped samples. The drastic changes in magnetic and transport behaviors are attributed to the introduction of sufficient charge carriers into the Sr_2IrO_4 matrix. The combined analyses suggest that the distorted Ir-O-Ir bond may not be an insurmountable barrier

in controlling the physical properties of Sr_2IrO_4 compounds. In the future, the most effective way to explore possible high-temperature superconductivity into the Sr_2IrO_4 system is to introduce more effective charge carriers into the IrO_2 plane.

ACKNOWLEDGMENTS

This work was supported by the Natural Science Foundation of Anhui Province (Grant No. 2008085MF204) and the National Natural Science Foundation of China (Grants No. 11874394 and No. 11904004).

[1] J. G. Bednorz and K. A. Muller, Z. Phys. B **64**, 189 (1986).

[2] Y. Kamihara, T. Watanabe, M. Hirano, and H. Hosono, J. Am. Chem. Soc. **130**, 3296 (2008).

[3] J. Linder and A. V. Balatsky, Rev. Mod. Phys. **91**, 045005 (2019).

[4] B. Lake, H. M. Rønnow, N. B. Christensen, G. Aeppli, K. Lefmann, D. F. McMorrow, P. Vorderwisch, P. Smeibidl, N. Mangkorntong, T. Sasagawa *et al.*, Nature (London) **415**, 299 (2002).

[5] Y. He, Y. Yin, M. Zech, A. Soumyanarayanan, M. M. Yee, T. Williams, M. C. Boyer, K. Chatterjee, W. D. Wise *et al.*, Science **344**, 608 (2014).

[6] O. Vafek and A. V. Chubukov, Phys. Rev. Lett. **118**, 087003 (2017).

[7] G. Y. Zhu and G. M. Zhang, Europhys. Lett. **117**, 67007 (2017).

[8] S. Zhu, L. Kong, L. Cao, H. Chen, M. Papaj, S. Du, Y. Xing, W. Liu, D. Wang, C. Shen *et al.*, Science **367**, 189 (2020).

[9] M. K. Crawford, M. A. Subramanian, R. L. Harlow, J. A. Fernandez-Baca, Z. R. Wang, and D. C. Johnston, Phys. Rev. B **49**, 9198 (1994).

[10] S. J. Moon, M. W. Kim, K. W. Kim, Y. S. Lee, J.-Y. Kim, J.-H. Park, B. J. Kim, S.-J. Oh, S. Nakatsuji, Y. Maeno *et al.*, Phys. Rev. B **74**, 113104 (2006).

[11] C. Wang, H. Seinige, G. Cao, J.-S. Zhou, J. B. Goodenough, and M. Tsoi, J. Appl. Phys. **117**, 17A310 (2015).

[12] G. Cao, J. Terzic, H. D. Zhao, H. Zheng, L. E. De Long, and P. S. Riseborough, Phys. Rev. Lett. **120**, 017201 (2018).

[13] B. Zwartsenberg, R. P. Day, E. Razzoli, M. Michiardi, N. Xu, M. Shi, J. D. Denlinger, G. Cao, S. Calder, K. Ueda *et al.*, Nat. Phys. **16**, 290 (2020).

[14] Fa Wang and T. Senthil, Phys. Rev. Lett. **106**, 136402 (2011).

[15] Z. Y. Meng, Y. B. Kim, and H.-Y. Kee, Phys. Rev. Lett. **113**, 177003 (2014).

[16] K. Nishiguchi, T. Shirakawa, H. Watanabe, R. Arita, and S. Yunoki, J. Phys. Soc. Jpn. **88**, 094701 (2019).

[17] A. W. Lindquist and H. Y. Kee, Phys. Rev. B **100**, 054512 (2019).

[18] Y. K. Kim, N. H. Sung, J. D. Denlinger, and B. J. Kim, Nat. Phys. **12**, 37 (2016).

[19] X. Chen, T. Hogan, D. Walkup, W. Zhou, M. Pokharel, M. Yao, W. Tian, T. Z. Ward, Y. Zhao, D. Parshall *et al.*, Phys. Rev. B **92**, 075125 (2015).

[20] T. Han, Y. Wang, J. Yang, L. He, J. Xu, D. Liang, H. Han, M. Ge, C. Y. Xi, W. K. Zhu *et al.*, Appl. Phys. Lett. **109**, 192409 (2016).

[21] C. Zhu, S. Liu, J. Cheng, B. Li, P. Dong, and Z. Wang, Europhys. Lett. **124**, 17004 (2018).

[22] S. T. Rodan, S. Yoon, S. Lee, K.-Y. Choi, G. Kim, J.-S. Rhyee, A. Koda, W.-T. Chen, and F. Chou, Phys. Rev. B **98**, 214412 (2018).

[23] P. Dong, X. Wang, J. Cheng, and X. Yan, Solid State Commun. **296**, 21 (2019).

[24] Y. Wang, L. Yao, J. Yao, W. Zhu, and C. Zhang, J. Supercond. Nov. Magn. **32**, 1583 (2019).

[25] Y. Hu, X. Chen, S.-T. Peng, C. Lane, M. Matzelle, Z.-L. Sun, M. Hashimoto, D.-H. Lu, E. F. Schwier, M. Arita *et al.*, Phys. Rev. Lett. **123**, 216402 (2019).

[26] C. Chen, Y. Zhou, X. Chen, T. Han, C. An, Y. Zhou, Y. Yuan, B. Zhang, S. Wang, R. Zhang *et al.*, Phys. Rev. B **101**, 144102 (2020).

[27] A. C. Larsen and R. B. von Dreele, GSAS software, Los Alamos National Laboratory Report No. LAUR 86-748 (1994), https://subversion.xray.aps.anl.gov/trac/pyGSAS.

[28] A. F. May, H. Cao, and S. Calder, Phys. Rev. Mater. **2**, 094406 (2018).